Wave-based Monitoring Processes in Granular Salt

M. Fam
Department of Earth Sciences, University of Waterloo

J.C. Santamarina
School of Civil and Environmental Engineering, Georgia Institute of Technology

M.B. Dusseault
Department of Earth Sciences, University of Waterloo

ABSTRACT

The goal of this paper is to evaluate the use of electromagnetic and mechanical waves to monitor the evolution of high-porosity granular salt during constrained loading, thermal changes, and moisture changes. Experimental results show that P and S wave velocities are better correlated with cumulative strain than with stress; the opposite is true for amplitude. This behavior can be explained at the micro-level using Hertzian and frictional contact laws. The complex dielectric permittivity is primarily sensitive to changes in moisture content; load and compaction-creep do not alter the prevailing polarization mechanisms. Other observations relate to creep rates, residual effects of temperature cycles and transient changes in wave velocity immediately after flooding. The magnitude of changes in the measured parameters support the monitoring of granular salt backfill with wave-based techniques.

Introduction

The disposal of nuclear waste requires safe isolation during the long decay time. Salt beds and crushed salt have been considered as host media and backfill because of the high creep rate of salt that leads to cavity closure, self-healing, time-dependent reduction in the hydraulic conductivity, and thereby, enhanced isolation of the waste (Hansen et al., 1993; Conley and Genin, 1990; WIPP project by Matalucci and Hunter, 1984).

The creep behavior of continuous media, such as rock salt, has been extensively studied. Granular salt inherits properties from the parent rock salt; however, the behavior of granular salt is strongly controlled by its particulate nature. Monitoring creep and the consequent changes in material characteristics presents unique challenges in discrete media, particularly in view of field applications where the access to shafts and tunnels is limited. This paper examines the use of wave-based techniques to study and to remotely monitor processes in high porosity granular salt.

Creep and Creep Mechanisms

Creep is usually defined as the time-dependent deformation of materials at constant stress and temperature. The creep rate $\dot{\varepsilon}$ is strongly affected by the state of stress σ', temperature, and moisture. At steady-state, the creep rate-temperature-stress relationship appears to be a characteristic of the material. This is not the case during transient conditions, where the creep rate is also a function of the loading history.

The creep of continuous materials can be explained by a combination of two processes: stable micro-fracturing and movement of dislocations (Ladanyi and Aubertin, 1990; Barber, 1990). Dislocations are extended forms of structural defects held together by atomic bonds. Microfractures are discrete planar flaws, across which atomic bonding is neglected. The principal creep mechanism in a *single-crystal* specimen is dislocation glide (Wanten, et al., 1993; see description in Table 1). The dominant creep mechanisms of *polycrystalline* salt specimens depend on the stress level and the temperature, and include (Table 1): dislocation glide, cross slip, dislocation climb, and diffusional creep (Coble creep and Nabarro-Herring creep). In addition, fluid-assisted pressure solution-precipitation is an important mechanisms in the presence of moisture.

Creep-maps have been proposed to delineate the regions corresponding to each mechanism. In general, two main regions are recognized: the "exponential-law regime" ($\dot{\varepsilon} \propto e^{-c}$) and the "power-law regime" ($\dot{\varepsilon} \propto \sigma'^{n}$). The boundary between both regimes is at $\sigma/G \approx 5 \cdot 10^{-4}$ where σ is the applied stress and G the shear modulus of salt (Munson and Dawson, 1984; Aubertin, 1993; Blum and Fleischmann, 1988). Proposed models are fitted to experimental data to determine the relevant parameters needed for design. For completeness, relevant mechanical, thermal, and electrical properties of rock salt are summarized in Table 2.

In the case of granular materials, grain crushing, rolling and slippage introduce additional deformation mechanisms (Feda, 1992). Creep of a granular matrix is termed "compaction creep" since it involves the reduction in void ratio. Different constitutive models have been proposed to predict strain rates in granular salt (e.g., Zhang et al., 1993; Holcomb and

Zeuch, 1990). Dislocation glide is reported to be the dominant creep mechanism in creep compaction of dry crushed salt, whereas pressure solution is important in the presence of moisture (Hunsche and Schulze, 1993). The level of moisture needed to activate the pressure solution mechanism in granular salt could be very small; the only requirement is that adsorbed films can act as conduits for continuous mass transfer of dissolved NaCl.

Waves - Particulate Media

Propagating mechanical waves can be used to examine the microstructure of a particulate medium. This is a small strain perturbation ($\gamma<10^{-5}$), hence, it does not alter the fabric. Velocity and attenuation reveal information about contacts and intergranular forces, which are determined by the state of stress and other internal processes (e.g., double layers). Experimental studies have shown that compressional and shear wave velocities are related to the state of effective stress through power relations (Cascante and Santamarina, 1996; Santamarina and Fam, 1995; Schultheiss, 1981; Roesler, 1979). Information on the effect of the microstructure on attenuation is limited.

The propagation of electromagnetic waves disturbs electrical charges and dipoles inside the material. Polarization in a steady-state field arises from a finite relative displacement of charges, and is defined as the dipole moment per unit volume. The dielectric permittivity is a complex parameter $\kappa^* = \kappa' - i\kappa''$. The real part κ' represents the polarizability of the medium, whereas the imaginary part κ''_{loss} captures polarization losses, κ''_{POL} and conduction losses κ''_{DC} (Fam and Santamarina, 1995):

$$\kappa''_{loss} = \kappa''_{POL} + \kappa''_{DC} \tag{1}$$

where

$$\kappa''_{DC} = \frac{\sigma_c}{2\pi f \varepsilon_o} \tag{2}$$

In this equation, f is frequency [Hz], σ_c is DC conductivity [Simens/m], and ε_0 is the permittivity of vacuum, $\varepsilon_0 = 8.85 \cdot 10^{-12}$ [Farad/m]. Table 3 highlights salient concepts and physical processes. Further information on the propagation of mechanical and electromagnetic waves in particulate media can be found in Fam and Santamarina (1995).

Table 1. Creep mechanisms.

Mechanism	Description	Form of Equation	Parameters	Reference
Dislocation Glide	Movement of dislocations along primary and secondary slip planes. It prevails a high stress σ/G >5·10^{-4}. Gliding continues until dislocations meet obstacles (high local stresses develop).	$\varepsilon' = A \cdot e^{-\left(\frac{B\sigma_d}{RT}\right)} \cdot e^{-\left(\frac{Q}{RT}\right)}$ *"exponential-law regime"*	Q = 100 kJ/mol	Munson and Dawson (1984)
Cross Slip	Obstacles may be overcome by the cross-slip of the screw components of dislocations. Thermally activated. Depends on loading direction. Prevails at high stress and low temperature.	proposed models also reduce to *exponential-law*		Aubertin 1993
Dislocation Climb	Obstacles along the gliding path may also be overcome by climbing. Sensitive to temperature and controlled by diffusion. More preponderant at higher temperatures. Prevails a low stress σ/G < 5·10^{-4}	$\varepsilon' = A \cdot \left(\frac{\sigma_d}{G}\right)^n \cdot e^{\left(\frac{-Q}{RT}\right)}$ *"power-law regime"*	Q = 100-200 kJ/mol n = 3 to 6	Munson and Dawson (1984)
Lattice Diff. (Nabarro-Herring)	Atoms flow within the material while vacancies flow in the opposite direction Dominant at high temperature T>300°C.	$\varepsilon' = K \frac{D}{d^2} \frac{\Omega \sigma_d}{kT}$	K = 10-14 D = 2.5·10^{-2} m^2/s Ω = 4.49·10^{-29} m^3	Evans and Wilshire (1993)
Boundary Diffusion (Coble)	Diffusion takes place along paths such as crystal or grain boundaries. Dominant at high temperature T>300°C.	$\varepsilon' = K \frac{D}{d^2} \cdot \frac{\delta}{d} \cdot \frac{\Omega \cdot \sigma_d}{k \cdot T}$	K= 40 δ·D = 6.2·10^{-10} m^3/s	Verrall et al. (1979)
Pressure Solution and Precipitation	Water enhances creep by facilitating dissolution and material transport. It involves three steps: (a) dissolution of material at interfaces under high normal stress, (b) diffusion along grain-boundary fluid, and (c) precipitation at interfaces under low normal stress.	$\varepsilon' = A \cdot V \cdot \frac{Z^*}{T} \cdot \frac{\sigma}{d^3 \varepsilon_v{}^a}$ $Z^* = D \cdot C \cdot \delta$	A = 11-33 V = 2.693·10^{-5} m^3 σ = stress in Pa a = 2-4	Spiers and Schutjens (1990)

Notation: R: 8.3143.10^{-3} kJ/K.mol; k: Boltzman constant; σ: Confining pressure; σ_d :deviatoric stress; G: Shear modulus; ε_V: Volumetric strain; Q: Activation energy; D: Diffusion coefficient; T: absolute temperature; C: crystal solubility; d: Grain diameter; δ: Boundary thickness

Table 2. Properties of sodium chloride.

Property	Value - Range	Notes/Reference
Specific gravity	G_s=2.14 - 2.16 (at 25 °C)	Kaufmann (1960) Sjaardema and Krieg (1987)
Shear strength c=shear intercept ϕ=angle shear resistance	c = 1.9 MPa, ϕ = 62° (porosity = 0.14) c = 1.1 MPa, ϕ = 33° (porosity = 0.26)	Fordham (1988)
Young's modulus	E=31 - 40 GPa	Kaufmann (1960) Morgan and Krieg (1990)
Shear modulus	G=10-16 GPa	Sjaardema and Krieg (1987)
Poisson's ratio	ν=0.25 - 0.27	Kaufmann (1960) Morgan and Krieg (1990)
Atomic Coordination #	N=6 (Simple cubic)	
Melting Temperature	T_m=1077 °K	Munson and Dawson (1984)
Thermal expansion	α_t=40.5 $\cdot 10^{-6}$ 1/C°	Kaufmann (1960)
Thermal conductivity	k_t=7.2 Watts/m °C	Kaufmann (1960)
Real permittivity	κ'=5.90 (10^2 to 10^{10} Hz)	Kaufmann (1960)
Imaginary permittivity	κ''< 1.0 f < 10^3 Hz κ''< 2.0 10^3 < f < 10^6 Hz κ''= 5.0 10^6 < f < 10^{10} Hz	Kaufmann (1960)
Wave velocity	V_p=4.59 km/s V_s=2.66 km/s	Gueguen & Palciauskas (1994)

Experimental Study

Mechanical and electromagnetic waves were used to monitor the evolution of granular salt specimens subjected to conditions that may potentially develop in field applications. Two grain sizes were tested: fine table salt (cubical particles of 0.25 mm average size) and angular-coarse crushed rock salt from the Sifto salt mine in Goderich, Ontario (3-10 mm average size; C_u=2.1 and C_c=0.8). Two oedometric cells were designed and built for these tests. The following sections describe the two cells and the experimental program. Stresses in this study were limited to 1.77 MPa. Results from Sjaardema and Krieg (1987) showed that the maximum induced stress on the crushed salt backfill is less than 0.50 MPa in the case of shaft and drift situations for the Waste Isolation Pilot Point project at a depth of 650 m.

<u>Large Oedometric Cell</u>

A large oedometric cell (steel, 195.6 mm diameter and 130.0 mm high) was built and used together with a high-capacity loading system (arm ratio=41.7) to simulate high overburden pressures and to avoid scale effects in the testing of the coarse granular salt. The cell was instrumented with P-wave transducers fixed to the base and to the top cap of the cell, three thermocouples placed at different elevations, and two dial gages used to measure vertical deformations (fig. 1). The cell has two hydro-ports at the base and top platens to allow flooding the material. A thermal jacket was designed to increase the internal temperature to 50°C. The computed radial strain in the steel shell at the maximum stress was $\varepsilon_r \approx 10^{4}$.

<u>Small Oedometric Cell</u>

The fine granular salt was tested in a small modified oedometric cell (100 mm diameter and 80 mm height) housed in a Wykeham-Farrance loading system (arm ratio=11). The small cell was instrumented with a coaxial termination dielectric probe HP-85070A connected to HP-8752A network analyzer to measure complex permittivity (0.02 GHz to 1.30 GHz), bender elements to transmit and receive shear waves, a

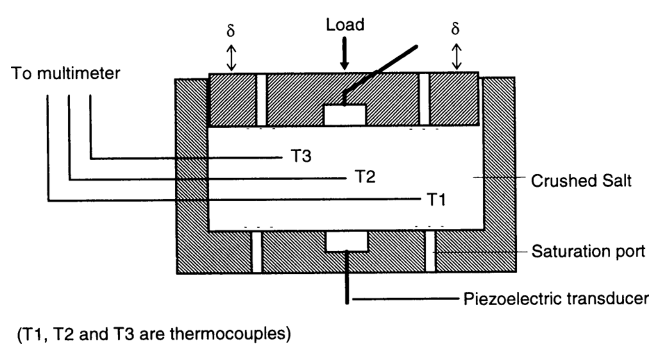

Figure 1. Large size oedometric cell and instrumentation (thermal jacket not shown).

Table 3. Waves: definition, characteristics, and physical significance.

	Mechanical wave	Electromagnetic wave
Definition	Compression waves (P-waves): particle motion in the direction of wave propagation. Shear waves (S-waves): particle motion perpendicular to the direction of wave propagation.	Electric and magnetic fields oscillating perpendicular to the direction of propagation.
Required material characteristics	Media with compressional stiffness (P-waves). Media with shear stiffness (S-waves).	Any media (including vacuum)
Characterizing parameters	Spectrum of wave velocity and attenuation.	Spectrum of complex permittivity (real and imaginary permittivity). The complex permittivity controls the velocity of electromagnetic wave propagation in a medium and its skin depth or attenuation.
Macro-level response	Volumetric strain and shear distortion.	Polarization of the material.
Micro-level response	Changes in interatomic distance, preserving local electroneutrality.	Relative displacement and rotation of electrical charges and dipoles.
Governing factors	Interparticle forces and contact stiffness in particulate materials.	Polarizability of: electrons, ions, molecules, bound water, interfacial-spatial, and double layers.
Physical significance (microlevel information)	Material stiffness, contact behavior, intergranular normal and shear forces, distribution of contact normals (geophysical applications), mechanical anisotropy, characteristic size.	Polarizability and conductivity of a medium.

thermocouple to monitor the temperature inside the cell, and a dial gage to measure vertical deformations (the overall geometry of this cell is a scaled version of fig. 1; a detailed description of the cell and the instrumentation can be found in Fam and Santamarina, 1995). This cell also permits controlling the vertical load, heating (hot air blower was used to increase the internal temperature to 50°C), and flooding (by adding water through the top porous stone).

Experimental Programs

Four experimental programs were completed as part of this study. The first three programs (G1, G2, and G3) involved testing fine and coarse granular salt in the oedometer cells. The loading sequences for the three tests and initial conditions are summarized in Table 4.

The fourth experimental program G4 was centered on dielectric permittivity measurements of fine granular salt at different moisture contents. Dry salt was mixed with different percentages of brine, and the dielectric permittivity was measured with the dielectric probe.

Results and Analyses

This section summarizes changes in measured parameters (vertical strain, wave velocity and permittivity) during different processes imposed on the specimens.

Process: Mechanical Loading

Strains and strain rates (quasi-static loading). Strains during staged loading were plotted against time for each load increment. All strain-time relationships showed primary creep behavior, i.e., decreasing strain rate with time. Data for specimen G2 are presented in fig. 2a (see similar data in Case et al., 1987). Specimen G3 was compacted to a lower initial void ratio than G2 (Table 4), and it exhibited a "pseudo" preloaded behavior, σ'_p, as reflected by the change in the slope of the e-log p curve (fig. 2b). Crushing sounds could be heard for the loading stage between σ'v=0.61 MPa and σ'v=1.23 Mpa in the G3 test.

The strain rate decreased linearly with time in log-log plots for all loading stages. The type of creep mechanisms can be inferred by fitting the data with the ε - σ' power relation and analyzing the power coefficient,

$$\varepsilon_t^{\cdot} = A_t \cdot \left(\frac{t}{t_o}\right)^m \cdot \left(\frac{\sigma'_d}{\sigma'_o}\right)^n \cdot e^{\left(\frac{-Q}{RT}\right)} \qquad (3)$$

where t is the creep time, σ'_d is the deviatoric stress, t_0=1 min. and σ'_0=1 kPa are normalization factors, A_t [1/s], m and n are model constants, and Q, R, and T are defined in Table 1. At constant temperature, A_t and $e^{(-Q/RT)}$ are constants and can be treated as a single parameter A_c [1/s]. A normalization step should be performed to estimate "m" under isothermal and isobaric conditions.

Creep rates at selected times are plotted versus stress in fig. 3 (G3 specimen). A linear relationship in a log-log plot between strain rate and applied stress is observed for different loading times. The fitting of eq. 3 to these data leads to $A_c=10^{-5.15}$ [1/s], m=-0.79, and n=1.56. The corresponding parameters for the G2 specimen are $A_c=10^{-5.10}$ [1/s], m=-0.83,

Table 4. Summary of experimental programs.

Program	Material and Test Cell	Initial Parameters	Measured Parameters	Cycles/Condition
G1	Fine - Small Cell	h_o = 56.4 mm e_o = 0.65 ρ_o = 1.33 g/cm^3 w/c_o = 0.19 %	Dielectric permittivity S-wave velocity Creep Temperature	1) Staged loading to 0.610 MPa 2) Heating by blowing hot air (T_{max} = 52.4 °C). Cooling 3) Saturation with water
G2	Coarse - Large Cell	h_o = 72.3 mm e_o = 0.54 ρ_o = 1.40 g/cm^3 w/c_o = 0.43 %	P-wave velocity Creep	1) Staged loading to 1.07 MPa 2) Unloading 3) Reloading to 1.53 MPa 4) Saturation with brine
G3	Coarse - Large Cell	h_o = 65.8 mm e_o = 0.493 ρ_o = 1.45 g/cm^3 w/c_o = 0.43 %	P-wave velocity Creep Temperature	1) Staged loading to 1.77 MPa 2) Heating with thermal jacket (T_{max} = 49.0 °C). Cooling 3) Saturation with brine
G4	Fine - High frequency probe Individual Samples	w/c_o = 0.19% to 15%	Dielectric permittivity	Dry samples mixed with different amounts of brine

and n=0.49. Note that a creep rate of $10^{-8}s^{-1}$ in a typical intact salt rock requires a stress ≈20-30 Mpa; however, similar strain rates take place in crushed salt at a confinement $\sigma \approx 0.5$ Mpa. If results are compared at the same confinement, the rate of creep in crushed salt can be as high as 10^7 times greater than in intact salt (estimated with empirical relations in Frayne et al. 1993; similar results were obtained by Korthaus, 1993).

The high-temperature Coble creep and Nabarro-Herring creep are excluded because tests were conducted at low temperatures (T_{lab}=20°C). Salt specimens were air-dry during the loading stage, with a moisture content ≈ 0.23%; this is sufficient to form extensive adsorbed layers, given the low specific surface of crushed salt. Hence, pressure solution must be expected (this is always the case in exposed crushed salt given its high permeability).

The potential for dislocation gliding, cross slip and dislocation climbing must be assessed in reference to contact stresses at the grain level, rather than in terms of average stress in the equivalent continuum. Assuming spherical geometry, the stress at the contact is estimated as $\sigma_{applied} \cdot (D^2 / d_{contact}^2)$. Because the area of contacts is very small during early stages of loading, these mechanisms are expected near particle contacts.

The power coefficient estimated from creep data with granular salt n_{grain} can be very different to that obtained for continuous specimens n_{cont} at the same boundary stress (consider a simple analysis consisting of integrating the strain rates in a sphere that was sliced into parallel disks). The ratio n_{grain}/ n_{cont} depends on the applied stress; the higher the stress level, the flatter the initial geometry of the contact and the closer the ratio is to 1.0. Therefore, it is not correct to directly infer the driving creep mechanism in particulate materials from the power coefficient determined from ε-σ' data.

Mechanical Waves: Velocity and Amplitude. The

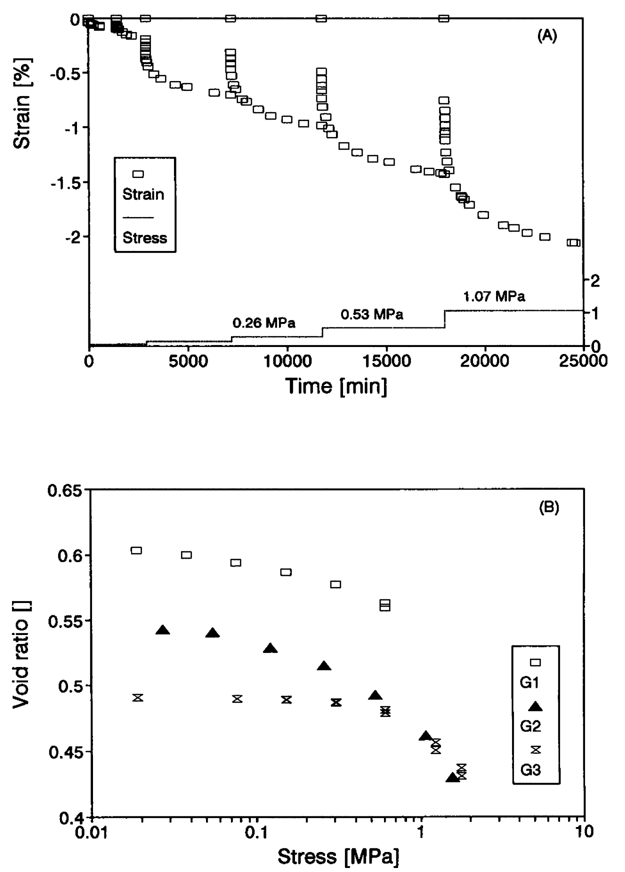

Figure 2. Stress-strain curves during loading: (a) stress-strain history for specimen G2, (b) e-log p curves for the three specimens.

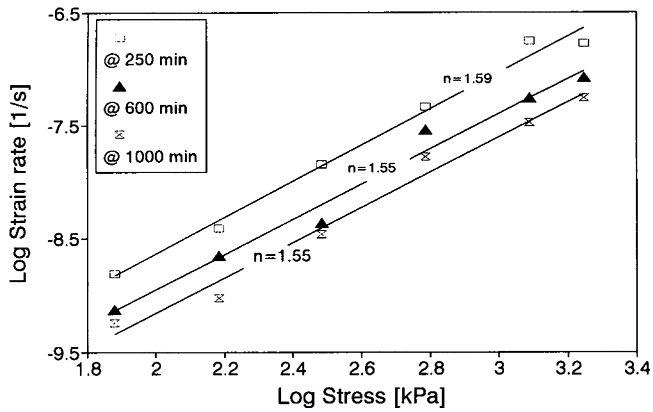

Figure 3. Strain rate-stress relationship - Specimen G3. Determination of the power coefficient "n."

change in velocity with time showed similar trends for the three tests (S-wave in G1, and P-wave in G2 and G3). Furthermore, the velocity-time trend during loading is similar to the strain-time trend: there is a sudden increase in velocity immediately upon loading, followed by a time-dependent increase, but at a decreasing rate (fig. 4-a: the test starts with a sitting load). The rate of change in velocity was observed to be independent of stress and linear with time in a log-log plot.

Two mechanisms are responsible for the increase in wave velocity in granular salt. The first one captures the change in fabric and contact stresses due to the change in the applied stress; whereas, the second mechanism accounts for the effect of time-dependent creep. Knowing that velocity in particulate media is governed by the state of stress, the following expression can be written to describe the previous two mechanisms during virgin loading:

$$V(\sigma', t_\sigma) = \xi_{v\sigma}\left(\frac{\sigma'}{\sigma'_o}\right)^{\chi_\sigma} + \xi_{vt}\left(\frac{t_\sigma}{t_o}\right)^{(1-\chi_t)} \quad (4)$$

where t_σ is the time from the beginning of the current load stage, and $\xi_{v\sigma}$, χ_σ, ξ_{vt}, and χ_t are material constants which can be inverted using regression analyses for velocity-stress and velocity rate-time relationships. Measured and modeled velocities using eq. 4 are shown in fig. 4a. Equation 4 yields infinite velocity when the stress and/or the time approaches infinity. A more complex equation with stress and time-dependent coefficients can be written to capture the finite asymptotic value of velocity. The proposed relationship applies for the range of stresses (<2 MPa) and times (<3 weeks) considered here.

The variation of wave amplitude with stress and time resembles the change in velocity (e.g., fig. 4b). Underlying mechanisms include increased number of contacts, grain flattening at contacts due to load and time dependent creep, displacement of adsorbed layers, and sytherisation (see results with lead shot in Cascante and Santamarina, 1996). Unfortunately, the change in the amplitude of the received signal reflects not only variations in attenuation, but also in the source and receiver coupling with the granular salt. Thus, damping can not be properly evaluated with the transmitter-receiver setup used in this study (see Fratta and Santamarina, 1996, for an alternative configuration).

The plot of S-wave velocity for all loading stages versus cumulative strain for specimen G1 shows no inflections or stages (fig. 5). P-wave velocity data from specimen G3 (also plotted in fig. 5) demonstrate the unique relationship between velocity and strain, except for the beginning of increment # 5 (1.23 MPa), when significant strain took place at constant velocity while grain crushing could be heard. The strong correlation between velocity and strain (independent of stress and time) deviates from prior studies that have favored the stress-dependency of stiffness in particulate materials. Both V_p-ε (G3 specimen) and V_s-ε (G1 specimen) show similar rates of velocity increase with strain, approximately 100 m/s per 1% strain. This is important for monitoring back-

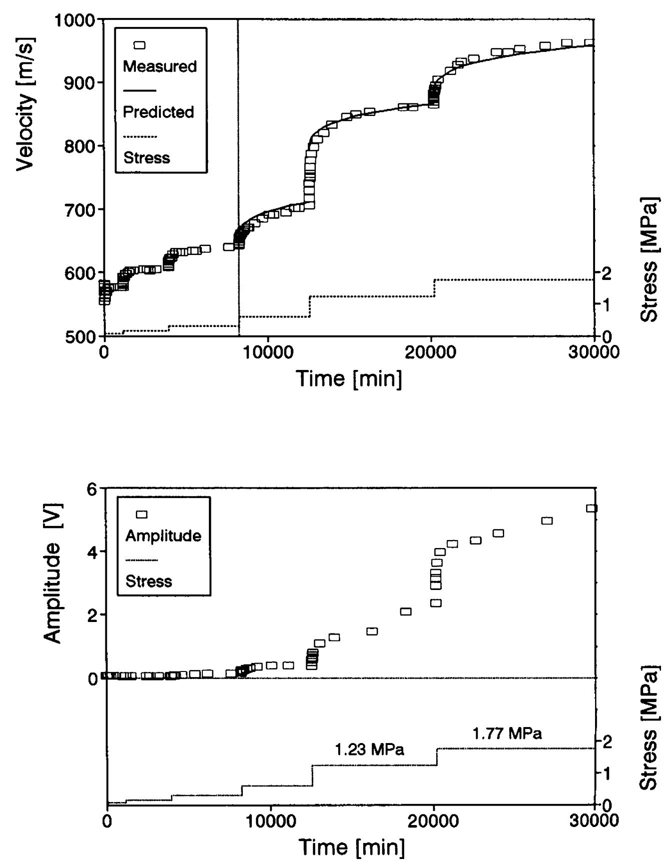

Figure 4. Mechanical waves during loading cycles - Specimen G3: (a) measured and predicted P-wave velocity and (b) peak-to-peak amplitude and stress history.

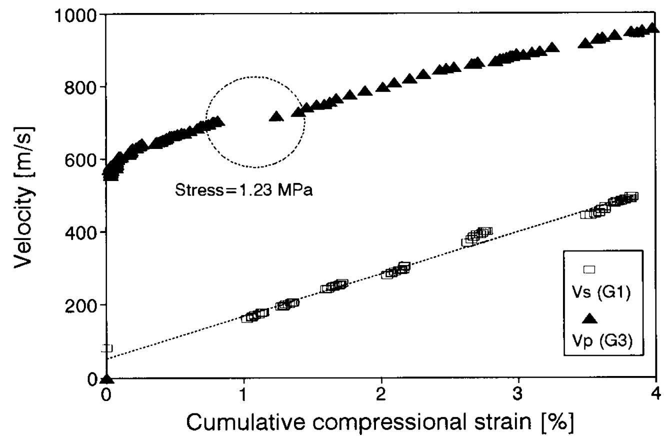

Figure 5. Velocity versus cumulative strain - Specimens G1 and G3 (Notice the discontinuity at $\sigma'_v = 1.23$ MPa).

fills with velocity measurements.

The standard velocity-stress power equations $V=\alpha\sigma'^{\chi}$ was fitted to velocities determined 24 hr. after loading (fig. 6). Fine granular salt gave a power coefficient χ=0.272. Data for test G3 (coarse particles) show a clear break after increasing the stress from 0.61 to 1.23 MPa. The power coefficient is 0.074 for low stress ($\sigma'_v < 0.61$ MPa) and 0.285 for high stress ($\sigma'_v > 0.61$ MPa). If the deformed geometry of elasto-plastic spheres is used to compute the low-strain elastic stiffness, the resulting velocity-stress exponent is χ=0.25; the exponent is higher for angular contacts and when the coordination number increases during compaction (Cascante and Santamarina, 1996).

Electromagnetic Waves: Complex Permittivity. Permittivity measurements for fine, air-dry salt during loading did not show significant changes with time or stress, ranging between κ'= 2.0 to 3.0 and virtually zero losses at 1.3 GHz. The small fluctuations in room temperature ± 1.5°C had a more significant effect: the higher the temperature, the lower the dielectric permittivity. Thermal agitation increases with temperature and reduces the polarizability of the medium.

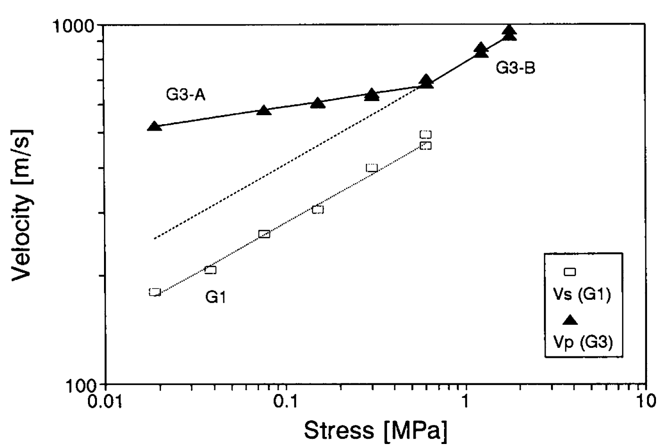

Figure 6. Velocity-stress curves - Speciments G3 and G1. Regression parameters are: region G3-A: ξ = 419.3 and X = 0.074; region G3-B: ξ =109.6 and X =0.285, (ξ =80.0 and X = 0.272.

Process: Heating and Cooling

Tests G1 and G3 included a heating cycle at constant vertical load, σ'_v. Monitored parameters included internal temperature in the specimen, vertical strain, wave velocity, and permittivity. The salt specimen was heated to approximately 50°C in both cases.

Strains. Temperature and deformation data for the G1 specimen are shown in fig. 7. Three deformation processes superimpose: oedometer shell thermal expansion (relieving σ'_h), salt thermal expansion, and increased creep compaction rate. These simultaneous deformation mechanisms were numerically modeled with finite differences. The following equation was used to represent the vertical strain in the granular salt specimen due to thermal dilation and creep:

$$\varepsilon(\sigma',t,T)=\alpha_e\Delta T-\int_0^t \dot{\varepsilon}^{\bullet}(\sigma',t,T)dt \qquad (5)$$

where α_e is the thermal expansion coefficient, and ΔT is the temperature change. The strain rate can be estimated using eq. 3.

$$\varepsilon^{\bullet}(\sigma',t,T)=A(\sigma',T_0)\cdot e^{\frac{Q}{R}\left(\frac{1}{T_0}-\frac{1}{T}\right)}\cdot\left(\frac{t}{t_0}\right)^m \qquad (6)$$

where T_0 is the room temperature in degrees Kelvin, and $A(\sigma',T_0)$ is a parameter that depends on the applied stress at room temperature. Numerical results are superimposed on the data in fig. 7. The simulation permits assessing the relative contributions of thermal dilation and creep, as shown in fig. 7-b. Similar data are presented in fig. 8 for the G3 specimen tested in the large oedometer. Even though heat cycles were at low temperature and of short duration, residual strains reached $\varepsilon_{res} \approx 0.3\%$ in both G1 and G3 specimens. During cooling, grain contraction can lead to contact loss and to the collapse of the microstructure. Hence, permanent strains may involve microstructural changes (Wawersik, 1988).

Mechanical Waves: Velocity and Amplitude. Wave velocity data exhibit similar trends to strain data in the two specimens G1 and G3. In agreement with the trend in strain, the value of V_s after the heat cycle is higher than before heating. Figure 7c shows a drop in shear wave velocity in G1 immediately after the initiation of the heating cycle. It is hypothesized that this drop is related to shell expansion and the reduction in the horizontal stresses σ'_h ($V_s \propto \sigma'^{\chi_v}_v \cdot \sigma'^{\chi_h}_h$; the independent assessment of temperature effects requires tests with constant-stress boundary conditions). A gradual increase in velocity can be observed in the G3 specimen (fig. 8b). The effect of temperature is also important on the amplitude of received signals, as shown in fig. 8c.

Electromagnetic Waves: Complex Permittivity. The change in the dielectric permittivity during the heat cycle confirmed the inverse relationship between permittivity and temperature discussed earlier.

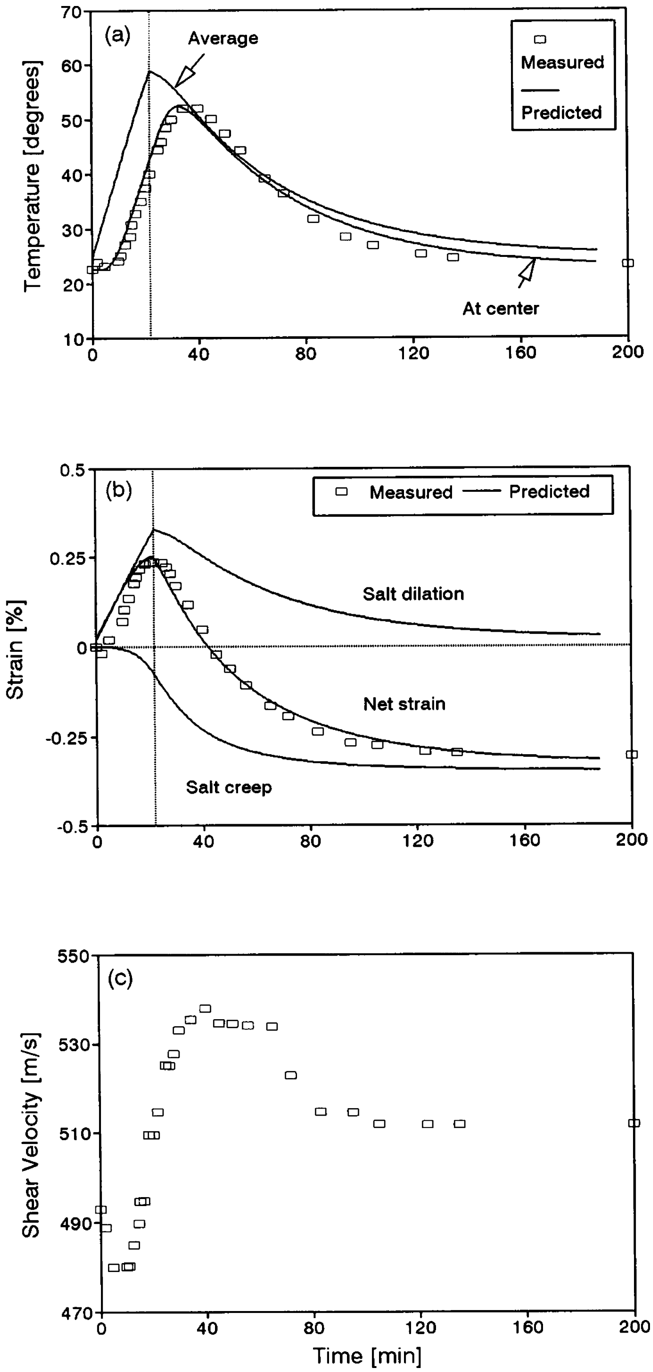

Figure 7. Heating-cooling cycle - Specimen G1: (a) measured and predicted temperatures, (b) measured and predicted vertical strains, and (c) measured shear wave velocity.

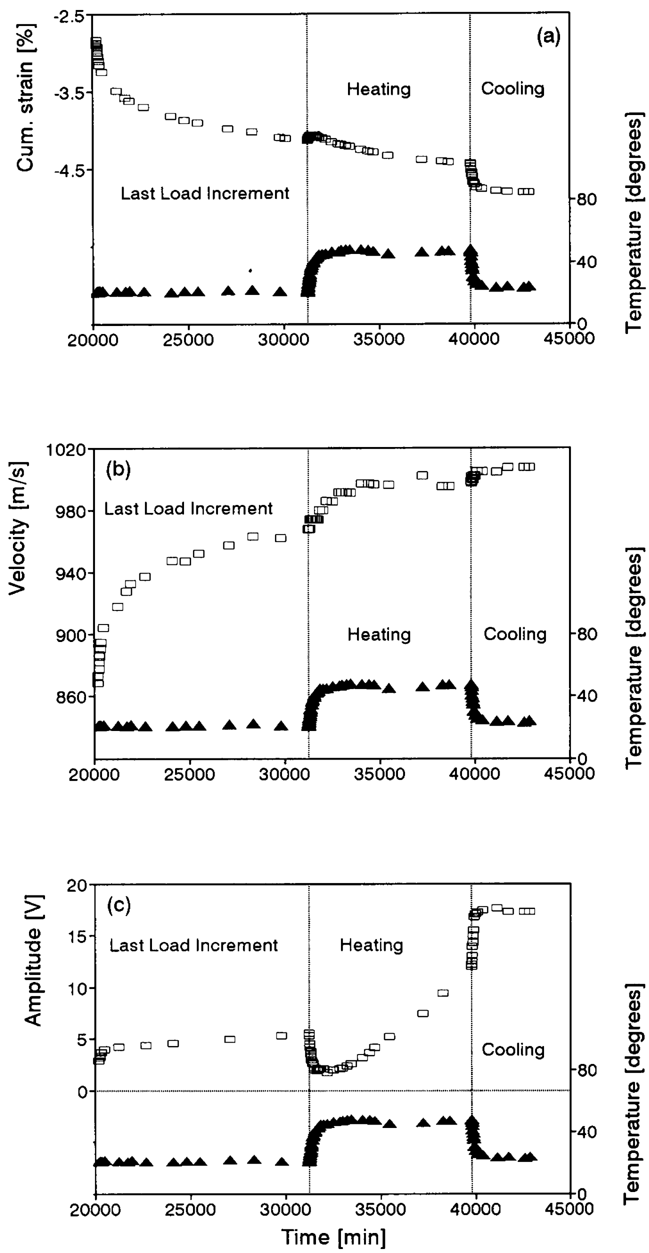

Figure 8. Heating-cooling cycle - Specimen G3: (a) vertical strain, (b) P-wave velocity, and (c) wave amplitude. The temperature history is also shown. This test was conducted at σ_v = 1.77 MPa.

Process: Flooding

Strains and Temperature. The three test programs G1, G2, and G3 involved a flooding cycle (see Table 4). The strain increases gradually with time during this cycle. High strain was recorded in the G1 test (strain≈12% after 8 hr.). This reflects the high solubility of salt in de-ionized water used to flood this specimen. Brine was used to flood specimens G2 and G3; in these cases, strains were lower than 3.0% after 10 days. The change in porosity due to pressure solution can be calculated for a regular packing of spheres assuming a simple geometrical model (Dusseault 1977). A significant reduction in porosity occurs ($\Delta n \approx 18\%$) at small percentages of mass transfer (1%). The corresponding increase in contact area reduces the mean contact stress significantly, and decreases the power coefficient n. The increase in strain rate with the increase in moisture content is also explained by pressure solution (Davidson and Dusseault, 1994).

The temperature inside sample G1 decreased about 2°C

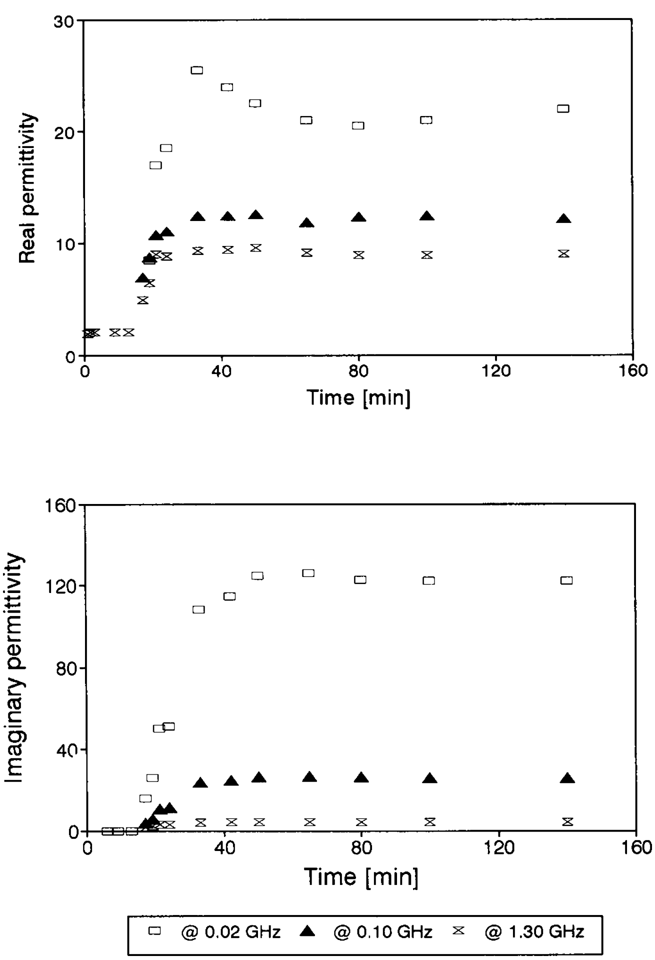

Figure 9. Dielectric permittivity at different frequencies - Specimen G1: (a) real permittivity, and (b) imaginary permittivity. This test was conducted at σ_V = 0.61 MPa.

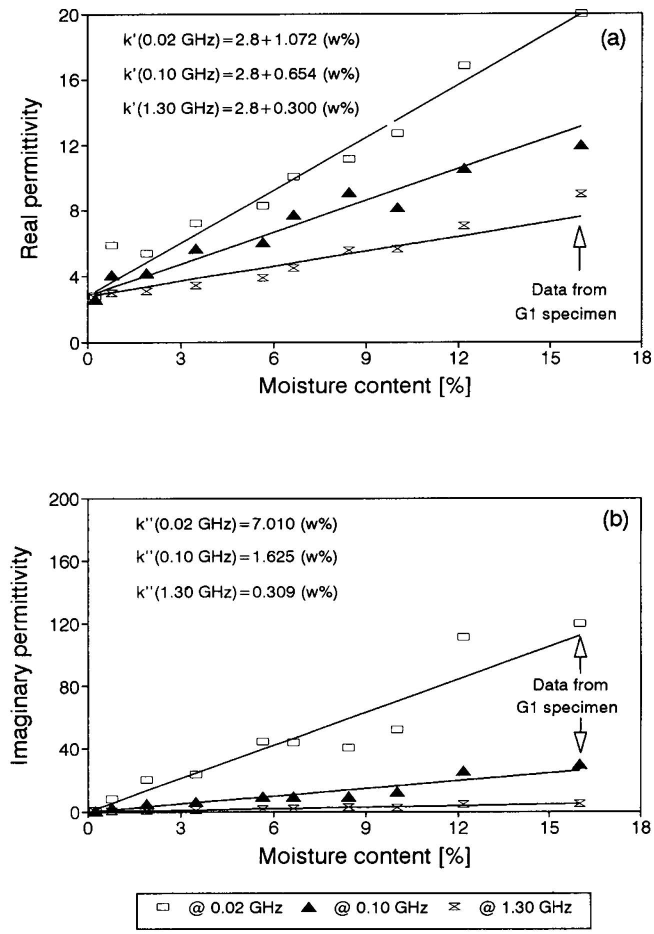

Figure 10. Complex permittivity and moisture content - Test G4: (a) real permittivity, and (b) imaginary permittivity. Data from specimen G1 are also shown.

as a result of the endothermic solubility of NaCl. However, no significant change in temperature was observed when brine was used in G2 and G3 specimens.

Mechanical Waves: Velocity and Amplitude. The velocity V_p dropped 5% immediately after flooding the specimen because of the increase in mass density of the flooded medium (Velocity $\propto$ Stiffness / Inertia). Fifty minutes after flooding, velocity started to increase at a rate greater than in the air-dry specimen.

Electromagnetic Waves: Complex Permittivity. The change in complex permittivity during the flooding cycle of specimen G1 is shown in fig. 9. Soon after water was added, it percolated through the specimen pores under gravity. The increase in real permittivity reflects the addition of dipolar water molecules. The very high conductivity of high concentration electrolytes leads to very high values of the imaginary permittivity (fig. 9b). Indeed, water-flooded granular salt is a high loss material, $\tan(\delta)=\kappa''/\kappa'>1$ for frequencies f<500 MHz; therefore, the skin depth is very small, e.g., $S_d \approx 0.1\ \lambda$.

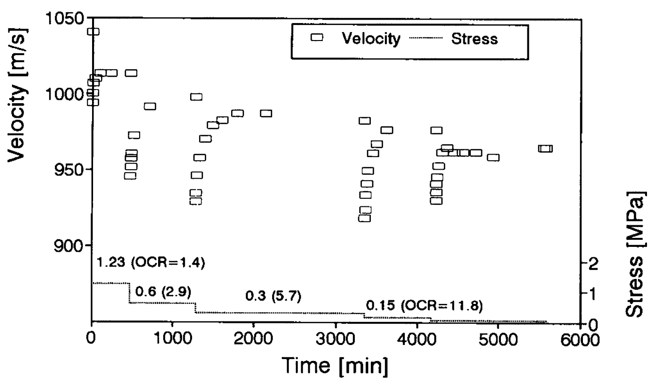

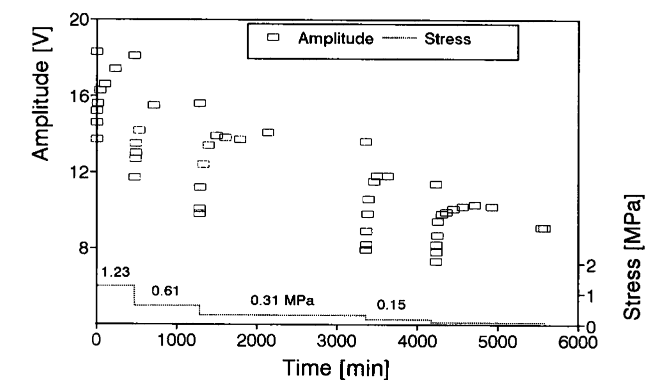

Figure 11. Wave propagation during unloading - Specimen G3: (a) wave velocity, and (b) peak-to-peak amplitude.

The effect of moisture content on permittivity was specifically addressed in test G4. Fine salt was mixed with different percentages of brine. The change in dielectric permittivity with moisture content is shown in fig. 10.

Process: Mechanical Unloading

The final unloading cycle was conducted after the flooding-drainage cycle was completed. Vertical strain, P-wave velocity and amplitude were monitored with time (specimen G3).

Mechanical Waves: Velocity and Amplitude. Elastic strain recovery took place immediately after unloading, and virtually no subsequent changes in strain were observed with time. However, this is not the case with P-wave, as observed in fig. 11: velocity and amplitude show a sudden drop immediately after unloading, followed by a gradual recovery.

A global 11% decrease in velocity and 67% in amplitude is observed with the reduction in stress. These results confirm that velocity is more sensitive to contact geometry than to contact forces, whereas the opposite applies to attenuation (this is consistent with Amonton's laws of friction). Similar conclusions were reached by Cascante and Santamarina (1996) from testing visco-plastic lead shot in a resonant column.

Final Structure. The final structure of specimens G2 and G3 showed slight cementation and the formation of conglomerates. Bonding between grains was observed with scanning electron microscopy for specimen G3.

Summary and Conclusions

A broad exploratory experimental study was conducted on granular salt to assess its behavior under potential field conditions in repositories. The effects of stress, temperature, and moisture content were measured. Special emphasis was placed on monitoring these processes with mechanical and electromagnetic waves. The most relevant observations follow.

Pressure solution must be expected in crushed salt due to its high moisture permeability. In addition, dislocation glide, cross slip and dislocation climb can take place even at low boundary stresses, given the high value of contact stresses. Contrary to intact salt, the creep mechanism can not be inferred directly from the average stress power coefficient because the particulate nature of crushed salt imposes a non-homogeneous stress distribution within each particle. The creep rate in granular salt can be several orders of magnitude greater than that of intact salt at the same confinement.

Wave propagation parameters can be used to monitor creep processes in granular salt. Wave velocity (P and S) in creeping granular materials such as crushed salt is controlled by the deformed geometry of particles rather than the state of stress. This is predicted with modified Hertzian models. On the other hand, attenuation is more sensitive to the state of stress than to contact area, in agreement with friction laws. The wave velocity increases ~100 m/s per each 1% strain. The amplitude of received signals is more sensitive than velocity to changes in stress and temperature.

The electromagnetic properties of salt are sensitive to changes in moisture content. The complex dielectric permittivity showed significant increase upon wetting, especially at low frequencies, highlighting the potential use of electromagnetic waves to detect changes in moisture content.

Acknowledgments

This study was conducted at the University of Waterloo, as part of a research program on wave-geomedia interaction and applications. Funding was provided by ANDRA, Agence Nationale pour la Gestion des Déchets Radioactifs, France.

References

Aubertin, M., 1993, On the physical origin and modeling of kinematic and isotropic hardening of salt, In Mechanical Behavior of Salt, Proc. Third Conference, France, p. 1-15.

Barber, D.J., 1990, Regimes of plastic deformation-processes and microstructures: an overview, In Deformation processes in minerals, ceramics and rocks, D. J. Barber and P. G. Meredith, eds., Unwin Hyman Ltd., London, p. 138-178.

Blum, W., and Fleischmann, C., 1988, On the deformation-mechanisms map of rock salt, Proc. 2nd conference on mechanical behavior of salt, Hanover, Germany, H. R. Hardy, and M., Langer, eds., Trans. Tech. Publications, p. 7-22.

Cascante, G. and Santamarina, J.C., 1996, Interparticle Contact Behavior and Wave Propagation, ASCE Geotechnical J., **122** (10), p. 831-839.

Case, J.B., Kelsall, P.C., and Withiam, J.L., 1987, Laboratory investigation of crushed salt consolidation, 28th US Symposium on rock mechanics, p. 189-196.

Conley, E., and Genin, J., 1990, Application of speckle methodology at a nuclear waste repository, Optical Testing and Metrology III, Recent advances in industrial optical inspection, SPIE, **1332**, p. 798-801.

Davidson, B.C., and Dusseault, M.B., 1994, An evaluation of salt strata and granular salt backfill for use as disposal medium and sealing material in a toxic solid civil waste repository, Proc. 16th Canadian Waste Management Conference, Calgary, Canada.

Dusseault, M.B., 1977, The geotechnical behavior of oil sands, Ph. D. Thesis, Civil Engineering Department, University of Alberta, Canada.

Evans, R.W., and Wilshire, B., 1993, Introduction to creep, The Institute of Materials, London.

Fam, M., and Santamarina, J.C., 1995, Study of geoprocesses with complementary wave measurements in an oedometer, Geotechnical Testing J., ASTM, **18** (3), p. 307-314.

Feda, J., 1992, Creep of soils and related phenomena, Elsevier Science Publication Company, Amsterdam.

Fordham, C.J., 1988, Behavior of granular halite for use as a backfill in potash mines, Ph. D. Thesis, Earth Sciences Department, University of Waterloo, Canada.

Fratta, D. and Santamarina, J.C., 1996, Waveguide Device for Multi-Mode, Wideband Testing Wave Propagation in Soils, ASTM Geotechnical Testing J., **19** (2), p. 130-140.

Frayne, M.A., Rothenburg, L., and Dusseault, M.B., 1993, Four cases in salt rock, In Mechanical Behavior of Salt, Proc. Third Conference, France, p. 457-468.

Gueguen, Y., and Palciauskas, V., 1994, Introduction to the physics of rocks, Princeton University Press, Princeton, New Jersey.

Hansen, F.D., Callahan, G.D., and van Sambeek, 1993, Reconsolidation of salt as applied to permanent seals for waste isolation pilot plant, In Mechanical Behavior of Salt, Proc. Third Conference, France, p. 309-321.

Holcomb, D.J., and Zeuch, D.H., 1990, Modeling the consolidation of porous aggregate of dry salt as isostatic hot pressing, J. Geophysical Research, **95** (B10), p. 15611-15622.

Hunsche, U., and Schulze, O., 1993, Effect of humidity and confining pressure on creep of rock salt, In Mechanical Behavior of Salt, Proc. Third Conference, France, 1-15, p. 223-234.

Kaufmann, D.W., 1960, Physical properties of sodium chloride in crystal, liquid, gas and aqueous solution states, In Sodium Chloride: The Production and Properties of Salt and Brine, D. W. Kaufmann, ed., Reinhold Publishing Corporation, NY, p. 587-626.

Korthaus, E., 1993, Measurement of crushed salt consolidation under hydrostatic and deviatoric stress conditions, In Mechanical Behavior of Salt, Proc. Third Conference, France, p. 297-308.

Ladanyi, B., and Aubertin, M., 1990, Rate effects in the deformation of rocks, Proc. First Materials Engineering Congress "Serviceability and Durability of Construction Materials." Part 1, Denver, USA, p. 433-451.

Matalucci, R.V., and Hunter, T.O., 1984, Geomechanical applications for the waste isolation pilot plant (WIPP) project, In Mechanical Behavior of Salt, Proc. First Conference, H. R. Hardy, and M. Langer, eds., p. 791-812.

Morgan, H.S., and Krieg, R.D., 1990, Investigation of an empirical creep law for rock salt that uses reduced elastic moduli, Rock Mechanics Contributions and Challenges, Hustrulid and Johnson, eds., Balkema, p. 965-972.

Munson, D.E., and Dawson, P.R., 1984, Salt constitutive modeling using mechanisms maps, Mechanical Behavior of Salt, Proc. First Conference, H. R. Hardy, and M. Langer, eds., p. 717-737.

Roesler, S.K., 1979, Anisotropic shear modulus due to stress anisotropy, J. Geotechnical Engineering, ASCE, **105** (GT7), p. 871-880.

Santamarina, J.C., and Fam, M., 1995, Changes in dielectric permittivity and shear wave velocity during concentration diffusion, Canadian Geotechnical J., **32** (4), p. 647-659.

Schultheiss, P.J., 1981, Simultaneous measurements of P & S wave velocities during conventional laboratory soil testing procedures, Marine Geotechnology, **4** (4), p. 343-367.

Sjaardema, G.D., and Krieg, R.D., 1987, A constitutive model for the consolidation of WIPP crushed salt and its use in analysis of backfilled shaft and drift configurations, SAND87-1977, Prepared by Sandia National Laboratories, Albuquerque, NM.

Spiers, C.J., and Schutjens, P.M., 1990, Densification of crystalline aggregates by fluid-phase diffusional creep, In Deformation Processes in Minerals, Ceramics and Rocks, D. J. Barber and P. G. Meredith, eds., Unwin Hyman Ltd., London, p. 334-353.

Verrall, R.A., Fields, R.J., and Ashby, M.F., 1979, Deformation mechanism maps for LiF and NaCl, J. American Ceramic Society, **60**, p. 211-216.

Wanten, P.H, Spiers, C.J., and Peach, C.J., 1993, Deformation of NaCl single crystals at $0.27T_m \leq T \leq 0.44T_m$, In Mechanical Behavior of Salt, Proc. Third Conference, France, 1-15, p. 103-114.

Wawersik, W.R., 1988, Alternatives to a power law creep model for rock salt at temperatures Below 160°C, Second Conference on Mechanical Behavior of Salt, Trans Tech publication, Germany, p. 103-128.

Zhang, C., Schmidt, M.M., and Staupendahl, G., 1993, Experimental and modeling results for compaction of crushed Salt, Mechanical Behavior of Salt, Proc. Third Conference, France, p. 377-388.